PHYSICAL REVIEW A VOLUME 46, NUMBER 1 1 JULY 1992

Hexagonal spatial patterns for a Kerr slice with a feedback mirror

G. D'Alessandro* and W. J. Firth
Department of Physics and Applied Physics, University of Strathclyde, 107 Rottenrow, Glasgow G4 0NG, Scotland, United Kingdom

(Received 26 December 1991)

We study analytically and numerically a very simple nonlinear optical system, a thin slice of Kerr material with a single feedback mirror. Theoretical analysis shows that for both a focusing and defocusing medium the plane-wave solution is unstable above a certain input intensity, and a hexagonal pattern of bright spots should form. The amplitude equations for this system are three coupled Ginzburg-Landau type equations. Numerical analysis confirms these results; moreover by further increasing the input intensity, the hexagonal solution becomes itself unstable and turbulent motion sets in.

PACS number(s): 42.50.Lc, 42.65.Jx, 42.65.Pc

I. INTRODUCTION

Many research groups have focused their attention on models where the spatial profile of the electromagnetic field is taken into consideration and the plane-wave approximation removed. A review and extensive bibliography of such studies have been published recently [1] as part of a special issue on transverse effects in nonlinear optics.

A very simple system of this type, namely a single slice of Kerr medium coupled to a single feedback mirror, is discussed here. Linear stability analysis of this system [2] reveals both static and dynamic instabilities. Numerical simulations in two transverse dimensions were recently presented [3] showing, in particular, the spontaneous appearance of hexagonal patterns. In this more extended treatment we give more complete and detailed numerical results for this problem, together with analysis in which we examine various levels of perturbation approach to the nonlinear behavior of the system. In particular, we derive appropriate amplitude equations of Ginzburg-Landau type for the problem, which are of a form typical in hydrodynamics [4,5].

The paper is setup as follows. In the following section we review the linear stability analysis for completeness, presenting threshold curves for various parameter values, including, in particular, the case of strong transverse diffusion of the excitation responsible for the Kerr effect, which will be shown in later sections to present both an interesting phenomenology and some rather surprising features. In Sec. III we proceed to the nonlinear problem, developing multiple scaling and other perturbation approaches on the basis of which we analyze the bifurcation structure for rolls and hexagons, the former being stable only in the one-transverse-dimension case. We derive the amplitude equations and discuss the parameter dependence of the coefficients in that equation.

Section IV concerns itself with numerical results, describing the methods adopted and the results obtained, and making generally satisfactory comparison with the analysis of preceding sections. In this work we are primarily concerned with pattern formation, so that a relatively sluggish medium is adequate, and the dynamical response is on the time scale of the medium response. Indeed, in the limit of slow response, we can neglect altogether the propagation time between the slice and the mirror, with very considerable economy of computer resource. Finally in Sec. V we conclude by considering further generalization of this work. We also consider some of the factors relevant to experimental observation of the sort of phenomena presented in this work.

II. BASIC MODEL AND STABILITY ANALYSIS

Many, even most, nonlinear optical systems incorporate counterpropagating beams, especially those based on Fabry-Pérot étalons, as are most lasers and many bistable devices. The extra degrees of freedom which bidirectional beams confer greatly increase the scope for complexity and pattern formation. In fact, no cavity structure is required, as Grynberg *et al.* [6] have shown, with in particular observations of hexagonal patterns in the far field of laser beams counterpropagating in a sodium vapor cell with no mirror or other external feedback. The far field is the Fourier transform of the pattern within the medium itself, and we can thus infer spontaneous symmetry breaking within the medium leading to hexagonal patterns, albeit necessarily constrained by the power, and thus diameter, limitations of the input beams.

Closely related also are the experiments of Giusfredi *et al.* on sodium vapor [7] in which the counterpropagating beam is provided by an external lens and mirror combination. Patterns exhibiting complex dynamics on the time scale of the round-trip to the mirror, but also on longer time scales, are observed, though limited in complexity by the input power available.

The basic model in the present work is rather simple, namely a thin antireflected slice of Kerr medium irradiated from one side by a spatially smooth beam, indeed a plane wave in the present and previous analysis [2] and in the numerical studies, with a plane feedback mirror behind to generate a counterpropagating beam in the Kerr slice (see Fig. 1). The detailed modulation stability analysis of this system has been presented elsewhere [2], building on a related problem involving a sequence of thin Kerr slices with free-space propagation between the slices, in which the crucial role of propagation in converting phase to amplitude modulation was identified [8].

The system that we have modeled is a good approximation of a direct band-gap semiconductor, such as InSb or GaAs: an electromagnetic field $\mathcal{E}$ excites electrons from the valence to the conduction band; once there, the electrons can diffuse (diffusion length l_D) or recombine with a free trap (time constant τ):

$$-l_D^2\nabla_\perp^2\tilde n + \tau\frac{\partial \tilde n}{\partial \tilde t} + \tilde n = \frac{\alpha\varepsilon_0}{h\nu}N_V|\mathcal{E}|^2,$$

where $\tilde n$ is the carrier density in the conduction band, α is the absorption cross section, N_V is the density of states in the valence band (we assume that it is not depleted), and ν is the frequency of the transition. The proportionality constant can be eliminated by suitably scaling the field

$$E = \sqrt{\frac{\alpha\varepsilon_0 N_V}{h\nu}}\,\mathcal{E}$$

so that the equation for the carrier density reads

$$-l_D^2\nabla_\perp^2\tilde n + \tau\frac{\partial \tilde n}{\partial \tilde t} + \tilde n = |E|^2.$$

Broadly similar equations would be obeyed by other types of mobile excitation which affect the refractive index in other kinds of media, e.g., liquid crystals [9].

The total electric field is the sum of a forward and backward field

$$E = \tilde F(\tilde{\mathbf x},t)e^{i(k_0\tilde z-\omega_0\tilde t)} + \tilde B(\tilde{\mathbf x},t)e^{i(k_0\tilde z+\omega_0\tilde t)} + \text{c.c.},$$

where $\tilde F$ and $\tilde B$ are slowly varying amplitudes. We assume that the carrier density changes (linearly) the refractive index of the medium, so that the electric field is phase modulated during the transit of the slice, but we neglect absorption: linear absorption does not change significantly the model and nonlinear absorption is an effect of higher order with respect to nonlinear phase modulation, provided we are sufficiently detuned from resonance. Finally, in order to simplify the model as much as possible we shall suppose that the slice is sufficiently thin as to allow the neglect of diffraction inside it (see end of this paragraph) and that diffusion washes out the grating formed by the forward and backward field inside the material. Under all these assumptions Maxwell's equations for the two fields have a very simple form

$$\frac{\partial \tilde F}{\partial \tilde z} = i\chi_0\tilde n\tilde F, \quad \frac{\partial \tilde B}{\partial \tilde z} = -i\chi_0\tilde n\tilde B, \tag{1}$$

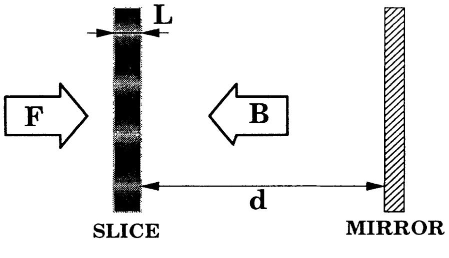

FIG. 1. Schematic diagram of the model. A thin slice of Kerr material, of thickness L, is illuminated from the left. The mirror, at a distance d, reflects this field back through the slice, thus closing the feedback loop.

while the equation for the carrier excitation density is

$$-l_D^2\nabla_\perp^2\tilde n + \tau\frac{\partial \tilde n}{\partial \tilde t} + \tilde n = |\tilde F|^2 + |\tilde B|^2, \tag{2}$$

where $\nabla_\perp^2$ is the Laplacian in the x and y directions. The modulus of $\chi_0 \equiv -k_0\gamma/2$ measures the strength of the nonlinearity while its sign determines the type: positive for focusing, negative for defocusing media. γ is the proportionality constant between the variation of the index of refraction and that of the carrier density. As the intensities of the two fields in Eq. (2) do not depend on z, we can suppose that the carrier density is uniform through the slice.

Finally, outside the material, the fields' evolutions are determined by Maxwell's equations in free space

$$\frac{\partial \tilde F}{\partial \tilde z} = \frac{i}{2k_0}\nabla_\perp^2\tilde F. \tag{3}$$

We can introduce adimensional quantities by scaling time with the recombination time and space with the diffusion length [keep in mind that $\tilde n$ is the excitation density per unit volume and that the electric fields' intensities are measured in the same units as $\tilde n$; see Eq. (2)]:

$$\begin{aligned}&|F|^2 = |\tilde F|^2 l_D^3, \quad |B|^2 = |\tilde B|^2 l_D^3,\\ &n = \tilde n l_D^3, \quad (x,y,z) = (\tilde x,\tilde y,\tilde z)l_D^{-1},\\ &d' = d l_D^{-1}, \quad L' = L l_D^{-1}, \quad t = \tilde t\tau^{-1},\end{aligned}$$

where L is the unscaled slice thickness and d is the unscaled slice-mirror distance. Equations (1)–(3) become

$$\begin{aligned}&\frac{\partial F}{\partial z} = i\frac{\chi}{L'}nF, \quad \frac{\partial B}{\partial z} = -i\frac{\chi}{L'}nB,\\ &-\nabla_\perp^2 n + \frac{\partial n}{\partial t} + n = |F|^2 + |B|^2,\\ &\frac{\partial F}{\partial z} = \frac{i\sigma}{2d'}\nabla_\perp^2 F,\end{aligned} \tag{4}$$

where $\chi \equiv \chi_0 L l_D^{-2}$ and $\sigma \equiv d/(k_0 l_D^2)$ is an adimensional parameter which measures the relative strength of diffraction versus diffusion (σ is small for strong diffusion). These equations admit a spatially uniform equilibrium point [2]:

$$|F|^2 = I_0, \quad |B|^2 = RI_0, \quad n = I_0(1+R), \tag{5}$$

where I_0 is the intensity of the forward (or pump) field and R is the reflectivity of the mirror. The uniform solution is linearly stable with respect to a perturbation of wave vector **K** for forward field intensities that are smaller than the value of the pump I_0 which satisfies

$$1 + K^2 - i\Omega = 2RI_0\chi \sin(\sigma K^2)e^{i\Omega t_R}, \qquad (6)$$

where t_R is the round-trip time from slice to mirror and back, $K = |\mathbf{K}|$, and Ω is the oscillation frequency of the perturbation. Equating the real and imaginary parts, we find that the oscillation frequency of the perturbation Ω is either zero or of the order of the round-trip time. In this work we consider only slow media so that dynamic instabilities ($\Omega \neq 0$) have a threshold much higher than the static instabilities ($\Omega = 0$) and can be ignored. Putting $\Omega = 0$ in Eq. (6) we obtain the instability threshold for the uniform solution with respect to such a nonoscillating perturbation of wave vector **K**:

$$|\chi|I_0 = \frac{1+K^2}{2R|\sin(\vartheta)|}, \quad \chi\sin(\vartheta) > 0, \qquad (7)$$

where $\vartheta \equiv \sigma K^2$. The inequality means that for focusing media $\vartheta \in \{(2m\pi, (2m+1)\pi), m = 0, 1, 2, \ldots\}$, while for defocusing media $\vartheta \in \{((2m-1)\pi, 2m\pi), m = 1, 2, \ldots\}$. As $\vartheta \propto K^2$ these conditions imply that the characteristic size of the instability pattern is smaller in a defocusing medium.

For fixed σ, the value of ϑ for which the threshold is minimum ϑ_{th} is given by

$$\tan(\vartheta_{\text{th}}) = \vartheta_{\text{th}} + \sigma. \qquad (8)$$

We can see that for small diffusion ($\sigma \gg 1$) the minimum instability threshold is at $\vartheta_{\text{th}} \simeq \pi/2$ for a focusing medium, $\chi > 0$, or at $\vartheta_{\text{th}} \simeq 3\pi/2$ for a defocusing medium, $\chi < 0$. Remembering the definition of σ and that space is scaled with the diffusion length we obtain that the characteristic length of the pattern is

$$L_{\text{pattern}} \simeq \begin{cases} \sqrt{\dfrac{8\pi d}{k_0}}, & \chi > 0 \\ \sqrt{\dfrac{8\pi d}{3k_0}}, & \chi < 0 \end{cases} \qquad (9)$$

($\sigma \gg 1$), i.e., it is dictated only by diffraction (the diffusion length being much smaller than this quantity). As a consequence, the minimum threshold intensity I_{th} is approximately independent of the slice parameters:

$$\chi I_{\text{th}} \simeq \frac{1}{2R} \qquad (\sigma \gg 1). \qquad (10)$$

The intensity scaling is such that χI_{th} is the light-induced phase shift due to the forward field alone [cf. (4) and (5)]. Thus (10) shows that this need be only of order half a radian if $R \simeq 1$. This is a reasonably modest phase shift, achievable in many types of medium.

If diffusion is dominant with respect to diffraction (i.e., $\sigma \ll 1$), then the size scale of the pattern becomes smaller and smaller compared to the diffusion length. In the case of a focusing medium, ϑ_{th} tends to zero for small σ and $\tan(\vartheta_{\text{th}})$ in Eq. (8) can be expanded in a Taylor polynomial. We obtain that

$$\vartheta_{\text{th}} \simeq (3\sigma)^{1/3} \qquad (\sigma \ll 1)$$

so that the characteristic length of the pattern is now

$$L_{\text{pattern}} \simeq 2\pi \left(\frac{l_D d}{\sqrt{3}k_0}\right)^{1/3} \qquad (\sigma \ll 1).$$

For a defocusing medium ϑ_{th} must be greater than π so that the length scale of the pattern does not change significantly with σ and is still approximately given by Eq. (9). Therefore, in both cases the ratio of the characteristic length to the diffusion length becomes smaller and smaller as the diffusion length increases so that the threshold intensity is bigger for smaller σ (see Fig. 2).

Before starting a nonlinear analysis of the stationary states it is worthwhile to explain more in detail what we mean by the requirement that the slice should be thin. It is a well-known fact that two counterpropagating beams in a slab of Kerr material may be an unstable system [10, 8], the plane-wave solution is unstable above a certain threshold with respect to perturbation of appropriate wave vector. For a self-focusing medium with no standing-wave-grating contribution to the refractive index change, the minimum threshold is given by $\pi/4$ in the same units as Eq. (10). For a defocusing medium the threshold is at least $\pi/2$. Thus in both cases the feedback-mirror instabilities have the lower threshold. Furthermore, the length scale of the pattern is, approximately,

$$L_{\text{pattern}} \simeq \sqrt{\frac{4\pi L_s}{k_0}},$$

where L_s is the thickness of the slab. If $L_s \ll d$, as in this case, then the size of the pattern due to counterpropagation instabilities is much smaller than that due to the feedback effect. If transverse diffusion is significant, as in the cases considered, the different space scales make the feedback-mirror instability have a much lower threshold intensity. We must remark, however, that for Gaussian beams, rather than plane waves, it may be power rather

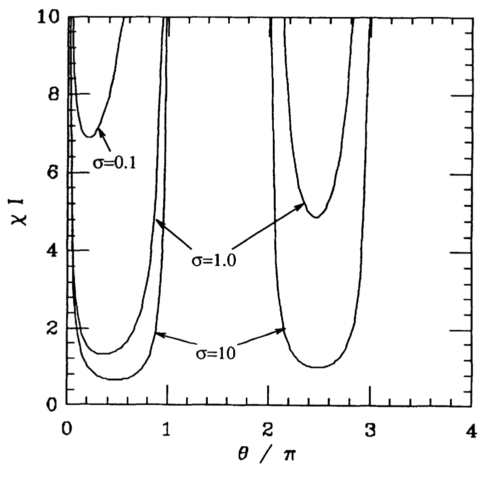

FIG. 2. Threshold curves for a focussing medium for three different values of σ. $R = 0.9$, $\chi > 0$.

than intensity which is the limiting factor: in such a case a small spatial scale for the pattern may make it easier to observe on a finite beam width.

III. NONLINEAR ANALYSIS

We first recast the problem as a single partial differential equation, albeit of infinite order, as opposed to two (rather trivial) ordinary differential equations, a partial differential equation, and a diffraction integral. The advantage is that the multiple-scaling analysis as presented by Dodd *et al.* [11] is couched in terms of dispersion relations for the linearized problem, and the transformation below adapts the present system to that approach. It may conceivably also lead to new numerical approaches, but that is not the primary objective.

In free space, the amplitude F of a field propagating in the positive-z direction obeys the fourth of Eqs. (4). In the present problem we formally integrate from slice to mirror and back to relate the incoming backward field to the outgoing forward field:

$$B(\mathbf{r},t) = \sqrt{R}\, e^{i\sigma\nabla_\perp^2} F_{\text{out}}(\mathbf{r}, t - t_R),$$

where F_{out} is the forward field immediately after going through the Kerr slice. Since propagation through the slice only multiplies the amplitude by $\exp(i\chi n)$, where $n(\mathbf{r},t)$ is the excitation density, and the time delay t_R can also be expressed via Taylor series as an operator, we can rewrite the preceding equation as

$$B(\mathbf{r},t) = \sqrt{R}\, F_{\text{in}} e^{i\chi n_0} e^{(i\sigma\nabla_\perp^2 - t_R\partial_t)} e^{i\chi\Delta n(\mathbf{r},t)} P(\mathbf{r},t).$$

Here F_{in} is the input amplitude, P is its profile, which is included here for generality--in particular as a potential starting point for analysis of Gaussian beam inputs—and n_0 is the constant, spatially uniform part of n, which can be commuted through the operators. We will here consider plane waves only so that $P = 1$ and can be dropped, and then the only operand is the exponential involving ΔN, the varying part of n, which we express as a perturbation series

$$\chi\Delta n(\mathbf{r},t) = \epsilon n_1(\mathbf{r},t) + \epsilon^2 n_2(\mathbf{r},t) + \epsilon^3 n_3(\mathbf{r},t) + \cdots . \tag{11}$$

χ has been absorbed into the n_i to simplify the ensuing expressions. We will be looking at low-order expansions of that exponential: ϵ is, naturally, a small parameter ($\epsilon > 0$) and will be the basis of the multiple-scaling perturbation expansion. The fact that Δn is of at least first order in ϵ follows from the fact that n is uniform below threshold, and our aim is to analyze the system close to threshold, i.e., where Δn is small.

For plane-wave input, the plane-wave steady-state solution n_0 is easily found (see Sec. II), and plays no role in the following. When n_0 is subtracted off, we find that Δn obeys the following infinite-order, nonlinear partial differential equation [cf. Eq. (4)]:

$$\begin{aligned}(-\nabla_\perp^2 + \partial_t + 1)\Delta n(\mathbf{r},t)\\ = R\chi I[|e^{i\sigma\nabla_\perp^2 - t_R\partial_t}\, e^{i\chi\Delta n}|^2 - 1], \quad I = |F_{\text{in}}|^2.\end{aligned} \tag{12}$$

Note that this is still an *exact* equation for plane wave, constant illumination. It represents the first objective of this analysis.

To this we must now apply the multiple-scales analysis formalism. The basis of the method is to separate fast and slow variations of the dependent variable(s) by introducing "slow" coordinates with variations of progressively higher order in ϵ, and doing a rigorous perturbation expansion in which one of the main criteria is that the higher-order n_i are always and uniformly smaller than the lower order terms. To ensure this, we at each order in ϵ have to make sure that there are no "secular" terms, which by definition are terms which grow linearly in time or space, and thus invalidate the perturbation series on scales of order ϵ^{-1}.

The slow scales are introduced by writing

$$\begin{aligned}\boldsymbol{\nabla}_\perp &= \boldsymbol{\nabla}_0 + \epsilon\boldsymbol{\nabla}_1 + \epsilon^2\boldsymbol{\nabla}_2 + \cdots ,\\ \nabla_\perp^2 &= \nabla_0^2 + 2\epsilon\boldsymbol{\nabla}_0\cdot\boldsymbol{\nabla}_1 + \epsilon^2(2\boldsymbol{\nabla}_0\cdot\boldsymbol{\nabla}_2 + \nabla_1^2) + \cdots ,\\ \partial_t &= \partial_0 + \epsilon\partial_1 + \epsilon^2\partial_2 + \cdots ,\end{aligned} \tag{13}$$

where the derivatives are with respect to new coordinates ($\mathbf{R}_i$,T_i), which are treated as *independent* of each other and especially of the basic "fast" coordinates ($\mathbf{r}$,t) to which the subscript 0 refers in (13). Thus a wave with an amplitude regarded as constant on fast scales can be modulated on the slower scales: indeed, we have to introduce the possibility of such a modulation to avoid secular terms.

The pump intensity I can be regarded as a function of ϵ expandable in a power series also:

$$I = I_0 p = I_0(1 + p'\epsilon + 1/2p''\epsilon^2 + \cdots), \tag{14}$$

where we anticipate that a minimum threshold intensity I_0 will be found below, and will coincide with I_{th} defined in Sec. II.

Setting

$$\hat{E} = e^{i\sigma\nabla_\perp^2 - t_R\partial_t}, \quad \hat{D} = 1 - \nabla_\perp^2 + \partial_t,$$

we have, at lowest order the linearization of (12),

$$\hat{L}n_1 = 0, \tag{15}$$

$$\begin{aligned}\hat{L}(\boldsymbol{\nabla},\partial_t) &= \hat{D} - iR\chi I(\hat{E} - \hat{E}^*)\\ &= \hat{D} + e^{-t_R\partial_t} 2R\chi I \sin(\sigma\nabla_\perp^2).\end{aligned}$$

Each successive approximation n_i makes its first appearance in an equation of the form

$$\hat{L}n_i = S_i, \tag{16}$$

where S_i are "source" terms involving n_j with $j < i$: (15) shows that $S_1 = 0$. These source terms include nonlinear terms, linear terms involving slow-variable derivatives, and mixed terms. Fortunately the last only come in at third and higher order in ϵ.

For $i = 1$ (15) may be solved by Fourier transforming: a nontrivial solution exists if

$$L(i\mathbf{K}, -i\Omega) = 0, \tag{17}$$

where $L(\mathbf{u}, v)$ is the function formed by replacing the operators on the left-hand side of (15) as indicated. Equation (17) is the dispersion relation for this problem and is a key element in the multiple scales analysis, especially following the Dodd *et al.* approach. Even though (12) is a rather complicated partial differential equation, the dispersion equation is quite easily obtained in this case: it is

$$L(i\mathbf{K}, -i\Omega) = 1 - i\Omega + K^2 - e^{i\Omega t_R} 2R\chi I_0 \sin(\sigma K^2) = 0$$

or, for a static instability, i.e., $\Omega = 0$,

$$2R\chi I_0 \sin(\vartheta) = 1 + K^2, \tag{18}$$

where I_0 is now the threshold intensity and K is the threshold wave vector. These two last equations are exactly those found in the linear stability analysis of the plane-wave solution [Eqs. (6) and (4)]. Therefore we can use the same notation introduced in Sec. II: we will indicate with the symbol I_{th} the minimum instability threshold, with K_{th} the most unstable wave vector, and with ϑ_{th} the corresponding value of ϑ.

The key to the multiple scales analysis is that the higher-order n_i in (16) can have wave vectors and frequencies which satisfy (18), i.e., they belong to the null space of $\hat{L}$. If the source term S_i contains any Fourier components in that null space, they are resonant and lead to linear temporal growth of n_i, which by definition is secular growth, and would invalidate the perturbation expansion (11) in times of order ϵ^{-1}. To avoid this, it is necessary that any secular source terms vanish identically: since these terms typically involve slow derivatives and nonlinear combinations of the amplitudes of the lowest-order approximation, this condition yields nonlinear partial differential equations for these amplitudes. The complex Ginzburg-Landau equation is the generic amplitude equation for spatially unstable dissipative waves [5], which is the case under consideration here.

At order ϵ^2 we obtain

$$\begin{aligned}\hat{L}n_2 = {} & [1 - 2R\chi\sigma I_0 \cos(\vartheta)]2\boldsymbol{\nabla}_0 \cdot \boldsymbol{\nabla}_1 n_1 \\ & -[1 + t_R 2R\chi I_0 \sin(\vartheta)]\frac{\partial n_1}{\partial T_1} \\ & +R I_0 \chi[(\hat{E}_0 n_1)(\hat{E}_0^* n_1) - \tfrac{1}{2}(\hat{E}_0 + \hat{E}_0^*)n_1^2] \\ & +2R\chi I_0 \sin(\vartheta) p' n_1 .\end{aligned} \tag{19}$$

Here the slow derivative terms can be obtained by substituting (13) into (15) and expanding in a Taylor series. Note that at minimum threshold the coefficient of the space-derivative term vanishes and it can therefore be dropped, because minimum threshold is the physically relevant condition. Thus at the minimum threshold the slow space dependence of the amplitude is arbitrary, which makes sense, since it just indicates that where the threshold is insensitive to $\mathbf{K}$, *any* slow spatial modulation of the amplitude of the wave is consistent with the threshold intensity.

The nonlinear third term in (19) comes from the $\exp(i\epsilon n_1)$ at second order. In the one-dimensional case considered by Dodd *et al.*, the nonlinear terms have spectral components at 0 and at $2K_{\text{th}}$, but not at K_{th}, so they introduce no secularity: then if (19) is obeyed, secular terms are eliminated at this order. Thus in one transverse dimension we do not get anything much from (19), and have to go to order ϵ^3 to obtain an amplitude equation.

With two transverse dimensions, however, we do have the possibility of secular nonlinear terms in (19). At the minimum threshold, where by definition $I = I_{\text{th}}$ and $\mathbf{K}^2 = K_{\text{th}}^2$, the coefficient of the slow spatial derivative term vanishes while stable, or at least time-independent, patterns will have no slow time derivative either. In that case the nonlinear terms in (19) can only be balanced by the p' term if secular terms are to be eliminated. We now evaluate these nonlinear terms, and show that they lead directly to hexagonally coordinated patterns.

Let φ be the azimuth variable in the transverse plane and write

$$\begin{aligned} n_1(\mathbf{r}) &= \int_0^{2\pi} d\varphi\, e^{i\mathbf{K}_\varphi \cdot \mathbf{r}} a(\varphi), \\ \mathbf{K}_\varphi &= K_{\text{th}}(\cos(\varphi), \sin(\varphi)), \end{aligned}$$

where $a(\varphi) = [a(\varphi + \pi)]^*$ is required so that n_1 be real everywhere. In principle $a(\varphi)$ can depend on the slow coordinates as well as φ, but we ignore that complication in this outline treatment.

We will need the Fourier transform of n_1

$$\tilde{n}_1(\mathbf{K}_2) = \frac{1}{K_2} a(\varphi)\delta(K_2 - K_{\text{th}}). \tag{20}$$

Here we have introduced K_2, as opposed to K_{th}, to keep track of the singularity in (20): we allow $K_2 \to K_{\text{th}}$ later. We also need the Fourier transform of n_1^2; this can be obtained from the Fourier transform of n_1 by making use of the convolution theorem and some algebra:

$$\tilde{n}_1^2(\mathbf{K}_2) = \frac{2}{\sqrt{3}K_{\text{th}}^2} a\left(\varphi + \frac{\pi}{3}\right) a\left(\varphi - \frac{\pi}{3}\right).$$

If $a(\varphi)$ is nonsingular, we cannot obtain a match in (19) between the nonlinear and linear terms in n_1, since the Fourier transform of n_1 is, by (20), proportional to a δ function. The only way out is for $a(\varphi)$ to be itself a δ function, of azimuth: then both linear and nonlinear terms are products of δ functions and can be matched. This evidently corresponds to a hexagonally coordinated pattern.

The next step in the multiple-scales analysis would be to complete the second-order calculation and use its result to evaluate the source terms at third order in ϵ. This, however, involves very lengthy algebra and it is convenient to use a simpler, but less rigorous approach. Using the result that we have just obtained we shall suppose that the carrier density is the sum of three rolls; their axes are at $2\pi/3$ from each other and their amplitudes are real functions of time, of order ϵ, a smallness parameter (different from the one used in the multiple-scales analysis) needed for bookkeeping that can, eventually, be eliminated:

$$n = \epsilon[A(t)\cos(\alpha) + B(t)\cos(\beta) + C(t)\cos(\gamma)], \tag{21}$$

$$\alpha = \mathbf{K}_1 \cdot \mathbf{x}, \quad \beta = \mathbf{K}_2 \cdot \mathbf{x}, \quad \gamma = \mathbf{K}_3 \cdot \mathbf{x},$$

where the wave vectors $\mathbf{K}_i$ have modulus $K_{\rm th}$, corresponding to the minimum threshold for the instability of the uniform solution and $\mathbf{K}_1 + \mathbf{K}_2 + \mathbf{K}_3 = \mathbf{0}$. This choice of carrier density is reasonable in the region near threshold. This suggests that we should also expand the pump parameter p in powers of ϵ, around one, as done in Eq. (14). However, we have not done this: we write the intensity as

$$I = I_{\rm th}p \tag{22}$$

and we do not put any restrictions on the values of p and suppose that the modulation of the carrier density is the only small quantity. There is no real justification for this perturbation-expansion approach, except that it works. The main caveat is that one should bear in mind that the results are "correct" only in the region near threshold. The only exception is when the three amplitudes A, B, and C are zero (uniform solution): in this case the expansion is correct whatever the value of the pump, but the results are rather trivial, being those derived in Sec. II. We can rewrite Eq. (12) using Eqs. (21) and (22) as

$$(-\nabla^2 + \partial_t + 1)\epsilon[A(t)\cos(\alpha) + B(t)\cos(\beta) + C(t)\cos(\gamma)]$$

$$= RI_{\rm th}p[|e^{i\sigma\nabla^2}e^{i\chi\epsilon[A(t-t_R)\cos(\alpha)+B(t-t_R)\cos(\beta)+C(t-t_R)\cos(\gamma)]}|^2 - 1]. \tag{23}$$

Our aim is to find the dynamical equations for the three amplitudes. We will not write down the intermediate steps in the computations as they are all very lengthy: the results of this section would have not been possible without the help of a computer algebra package (we used MAPLE) and even so much manual calculation was needed. What follows is a schematic description of the procedure that we have devised.

(i) Expand $e^{i\chi n}$. Expand $e^{i\chi n} = \exp\{i\chi\epsilon[A\cos(\alpha) + B\cos(\beta) + C\cos(\gamma)]\}$ in a Taylor series around $\epsilon = 0$ up to third order in ϵ. This expression contains terms with wave vectors of moduli $0, K_{\rm th}, \sqrt{3}K_{\rm th}, 2K_{\rm th}, \ldots$.

(ii) Evaluate $e^{+i\sigma\nabla^2}e^{i\chi n}$. The propagator operator in the space of functions $e^{i\sigma\nabla^2}$ becomes $e^{-i\sigma K^2} = e^{-i\vartheta}$ in Fourier space. This must be applied to each term in the expansion of $e^{i\chi n}$, i.e., we must multiply the uniform terms ($K = 0$) by 1, the terms with wave vector $K_{\rm th}$ by $e^{-i\vartheta_{\rm th}}$, the terms with wave vector $\sqrt{3}K_{\rm th}$ by $e^{-i3\vartheta_{\rm th}}$, and so on, i.e., each term in the expansion is an eigenfunction of the propagation operator.

(iii) Evaluate $|e^{+i\sigma\nabla^2}e^{i\chi n}|^2$. Take the modulus square of the expression obtained at point (ii), again keeping terms only up to third order in ϵ. Another simplification that reduces enormously the number of terms is that we are interested only in resonant terms, i.e., only in terms that have wave vectors of modulus $K_{\rm th}$: writing Eq. (21) for the amplitude of the carrier density we have implicitly supposed that the nonresonant terms are negligible (see later for a discussion of this hypothesis). The resulting expression has this form:

$$\begin{aligned} 1 &+ [\epsilon D_{11} + \epsilon^2 D_{12} + \epsilon^3 D_{13}]\cos(\alpha) \\ &+ [\epsilon D_{21} + \epsilon^2 D_{22} + \epsilon^3 D_{23}]\cos(\beta) \\ &+ [\epsilon D_{31} + \epsilon^2 D_{32} + \epsilon^3 D_{33}]\cos(\gamma), \end{aligned}$$

where the $D_{i,j}$ are functions of the amplitudes A, B, C and of $\vartheta_{\rm th}$.

(iv) Equate the right-hand side and the left-hand side of Eq. (23) and put $\epsilon = 1$ *(there is no need for bookkeeping now).* The final result is

$$\begin{aligned} \frac{\partial A}{\partial t} &= \mu A + \eta BC - [\zeta_1 A^2 + \zeta_2(B^2 + C^2)]A, \\ \frac{\partial B}{\partial t} &= \mu A + \eta AC - [\zeta_1 B^2 + \zeta_2(A^2 + C^2)]B, \\ \frac{\partial C}{\partial t} &= \mu A + \eta AB - [\zeta_1 C^2 + \zeta_2(A^2 + B^2)]C; \end{aligned}$$

$$\mu = 2R\chi I_{\rm th}\sin(\vartheta_{\rm th})(p - 1),$$

$$\eta = RI_{\rm th}p\chi^2[1 - \cos(\vartheta_{\rm th})],$$

$$\zeta_1 = \tfrac{1}{4}RI_{\rm th}p\chi^3[3\sin(\vartheta_{\rm th}) - \sin(3\vartheta_{\rm th})],$$

$$\zeta_2 = \tfrac{1}{2}RI_{\rm th}p\chi^3[2\sin(\vartheta_{\rm th}) - \sin(2\vartheta_{\rm th})].$$

As stated in Sec. II, for focusing media ($\chi > 0$) $0 < \vartheta_{\rm th} < \pi/2$, while for defocusing media ($\chi < 0$) $\pi < \vartheta_{\rm th}3\pi/2$. It follows that the four parameters μ, η, ζ_1, and ζ_2 are all positive quantities independently of the sign of the nonlinearity. The left-hand side of these equations is evaluated at time t, while the right-hand side at time $t - t_R$. If the recombination time of the carriers is very long compared to the return-trip time t_R, then we can neglect this detail and evaluate both sides of these equations at the same time. In fact, multiple-scales analysis shows that the correct time constant for the amplitude equations is $\mu[1 + 2t_R\sin(\vartheta)]$: this term reduces to μ if the return-trip time is much smaller than the recombination time.

Finally, the hypothesis that A, B, and C are real quantities is not important: its main purpose is to simplify the algebra and can be easily dropped. We can write the carrier density as

$$n = (Ae^{i\mathbf{K}_1\cdot\mathbf{x}} + Be^{i\mathbf{K}_2\cdot\mathbf{x}} + Ce^{i\mathbf{K}_3\cdot\mathbf{x}} + \text{c.c.})/2$$

and obtain three Ginzburg-Landau type equations for the complex amplitudes

$$\begin{aligned} \frac{\partial A}{\partial t} &= \mu A + \eta B^* C^* - [\zeta_1 |A|^2 + \zeta_2(|B|^2 + |C|^2)]A, \\ \frac{\partial B}{\partial t} &= \mu A + \eta A^* C^* - [\zeta_1 |B|^2 + \zeta_2(|A|^2 + |C|^2)]B, \\ \frac{\partial C}{\partial t} &= \mu A + \eta A^* B^* - [\zeta_1 |C|^2 + \zeta_2(|A|^2 + |B|^2)]C. \end{aligned} \tag{24}$$

Similar equations have been obtained in a number of fields of physics, from hydrodynamics [4, 12] to flame physics [13]. This should not be surprising as they describe the most simple form of interaction of three waves whose wave vectors satisfy the condition: $\mathbf{K}_1+\mathbf{K}_2+\mathbf{K}_3 = \mathbf{0}$. The first term is the linear decay or growth of the wave; the second is due to the sum of the other two waves ($\mathbf{K}_1 = -\mathbf{K}_2 - \mathbf{K}_3$). It is a characteristic feature of two-dimensional systems as all three waves need to be present in order for this term to be active. Finally, the last term is the only form of third-order nonlinearity which is resonant and represents a saturation of the triad coupling.

It is possible to analyze the stationary states of this model exactly in the same way as in Ref. [4] (see Fig. 3), but the form of the coefficients poses some constraints on the solution types (there are no mixed states of hexagons and rolls) and their stability. There are three kinds of stationary solutions: (i) The uniform solution ($A = B = C = 0$) is stable for $p < 1$, unstable otherwise (line U in Fig. 3); (ii) rolls (curve R in Fig. 3), given by

$$A = \mathcal{A}e^{i\varphi}, \quad B = C = 0,$$

$$\mathcal{A} = \frac{1}{|\chi|}\sqrt{\frac{8(p-1)\sin(\vartheta_{\text{th}})}{3\sin(\vartheta_{\text{th}}) - \sin(3\vartheta_{\text{th}})}}, \quad \varphi \in [0, 2\pi)$$

and any cyclic permutations exist for $p > 1$ and are always unstable. The point μ_3 in Ref. [4] where the rolls become stable cannot be reached in our model whatever the value of the pump; (iii) hexagons, given by

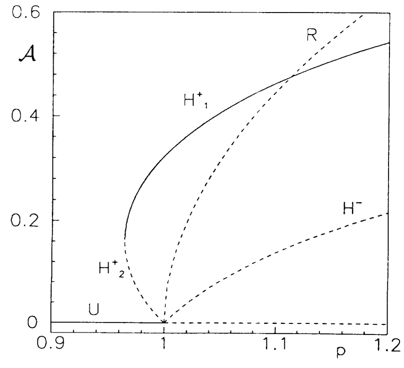

FIG. 3. Bifurcation diagram of Eqs. (24). The continuous lines indicate stable solutions, the dashed lines unstable ones. $R = 0.9$, $\sigma = 10$, and $\chi = 1.0$.

$$A = B = C = \pm\mathcal{A}, \quad \mathcal{A} \in \mathbb{R}^+, \quad p = \frac{1}{1 \pm T_1\mathcal{A} + T_2\mathcal{A}^2}; \tag{25}$$

$$T_1 = \chi\frac{\sin^2(\vartheta_{\text{th}}/2)}{\sin(\vartheta_{\text{th}})},$$

$$T_2 = -\chi^2\frac{11\sin(\vartheta_{\text{th}}) + 4\sin(2\vartheta_{\text{th}}) + \sin(3\vartheta_{\text{th}})}{8\sin(\vartheta_{\text{th}})}.$$

The ± sign in the equation for p corresponds to the ± sign in the amplitudes. As T_1 and T_2 are, respectively, positive and negative independently of the sign of the nonlinearity, the bifurcation diagram (Fig. 3) is the same for both focusing and defocusing media. This solution exists only if

$$p > \frac{4T_2}{4T_2 + T_1^2}.$$

The plus sign in Eq. (25) gives the two curves H_1^+ and H_2^+ in Fig. 3. The upper branch is always stable, the lower branch is unstable. The minus sign, instead, gives the curve H^-; this solution is phase unstable. The point μ_4 in Ref. [4], where even the solutions on the H_1^+ curve become unstable, cannot be reached in our model whatever the value of the pump.

We have checked numerically the amplitude of the hexagons and rolls for various values of σ in the region near threshold (see Sec. IV for a detailed description of the numerical method used). For both hexagons and rolls we have started our simulations well above threshold and we have decreased the amplitude step by step until we were below threshold, making sure that each step was long enough so that equilibrium could be reached. We have used a two-dimensional version of the program for the hexagons (256 x 256 points grid) and a one-dimensional version for the rolls (256 points). Figure 4 is a typical example of the output of one such run. The pump intensity is decreased and the carrier density relaxes towards an equilibrium value. The relaxation time increases as we reach the instability threshold of the hexagons. The inset shows a plot of the relaxation time versus the pump intensity and provides an estimate of the threshold value. The agreement with the theoretical estimates is quite good for high values of σ (weak diffusion), but there is definitely no agreement between theory and simulations for $\sigma = 0.1$ (strong diffusion) (see Fig. 5). Why is this? The main approximation in the procedure outlined above is that the carrier density has Fourier components only with the most unstable wave vector K_{th}. This component, however, acts as a source term for higher-order harmonics. For example, the A component of Eq. (21) generates a second-harmonic term source term given by

$$(\chi A)^2 \sin^2(2\vartheta_{\text{th}}).$$

This is very small for weak diffusion: in this case $\vartheta_{\text{th}} \simeq$

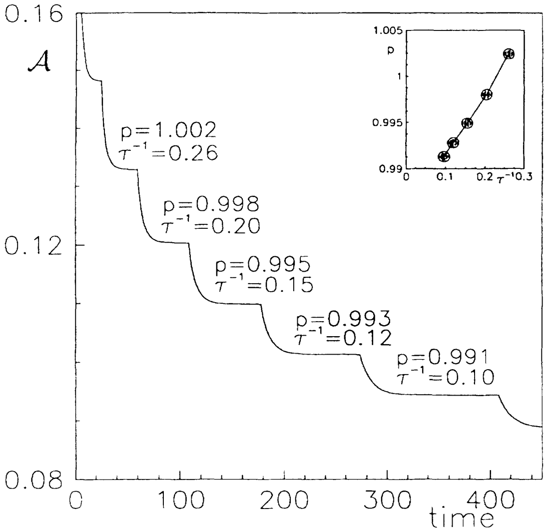

FIG. 4. Plot of the modulation amplitude $\mathcal{A}$ as function of time. The intensity of the pump field p is decreased step by step. τ is an estimate of the relaxation time. The inset shows τ vs p. $\sigma = 0.1$, $\chi = 1.0$, $t_R = 0.05$.

$\pi/2$. For strong diffusion, however, ϑ decreases away from $\pi/2$, and this term is not negligible. This suggests that we can obtain a better fit between theory and numerical simulations by using two Fourier components in the expression for the carrier density. We have checked this hypothesis in the case of the rolls. The procedure that we have followed is similar to the recipe for obtaining the amplitudes equations, Eqs. (24). The main differences are (a) we are dealing with a one-dimensional case; (b) the carrier density has two Fourier components:

$$n = \epsilon[A_1 \cos(K_{\text{th}}x) + A_2 \cos(2K_{\text{th}}x)]; \tag{26}$$

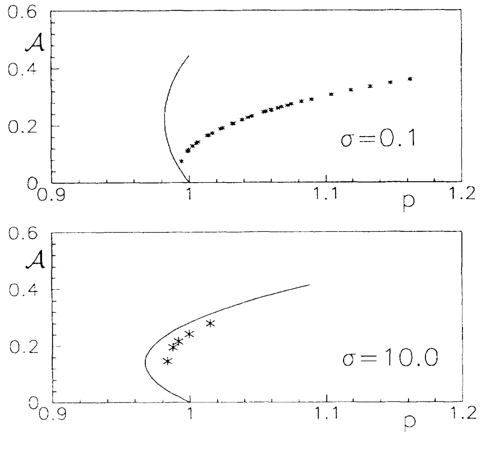

FIG. 5. Amplitude of the A mode for the hexagonal H^+ stationary solution of Eqs. (24) vs the pump parameter p. $R = 0.9$ and $\chi = 1.0$. The stars are the amplitudes obtained numerically.

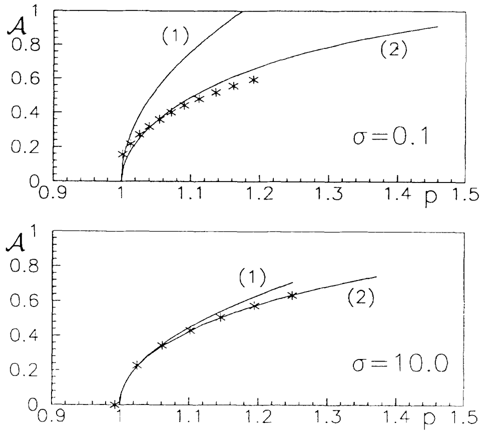

FIG. 6. Amplitude of the rolls vs the pump parameter p considering one (1) or two (2) harmonics in the carrier density. $R = 0.9$ and $\chi = 1.0$. The stars are the amplitudes obtained numerically.

(c) we are interested only in the equilibrium state so that the amplitudes A_1 and A_2 are time independent quantities.

Taking into account two Fourier components requires a great deal of algebra. Again we had to use MAPLE and the final plot has been obtained by a FORTRAN program generated automatically by it. The final expression for the equilibrium value of the carrier density is very long and there is not much point in writing it down. The agreement between theory and numerical simulations is good even for $\sigma = 0.1$ (Fig. 6).

Concluding, we have seen that linear stability analysis provides only limited information on the phase space of the system: the instability threshold for the uniform solution. Nonlinear analysis, however, shows that the system has other equilibrium solutions, hexagons and rolls; moreover, their amplitudes are governed (to first order) by Ginzburg-Landau-type equations, in a similar fashion to many problems in other branches of physics.

IV. NUMERICAL ANALYSIS

Linear and nonlinear analysis give a rough map to the parameter space of the Kerr-slice model. However, numerical analysis is fundamental to get a more complete understanding of it and to check that the approximations done in the analytical study are correct. Therefore we have developed a numerical code to integrate the Kerr-slice equation. Since this model system is relatively simple, the code can run at a reasonable speed on computer work stations of the class of a Sun Sparcstation1.

Both the electric field and the carrier density are represented by square arrays (typical dimensions in our simulations have been 128 x 128 or 256 x 256 points). The propagation of the electric field from the slice to the mirror and back (free-space propagation) is handled by a fast-Fourier-transform routine:

(1) Fourier transform $e^{i\chi n(t)}$.

(2) Multiply the result by $e^{-i\sigma K^2_{i,j}}$, where $K_{i,j}$ is the wave vector in Fourier space associated with the grid point (i,j).

(3) Anti-Fourier transform, take the modulus square, and multiply by the reflectivity of the mirror.

At the end of this step we have the backward field at time $t + t_r$. This quantity is stored for later use as the source term in the equation for the carrier density n.

The equation for the carrier density, instead, is integrated with an implicit-explicit method, the Hopscotch algorithm [14]. The source term, the sum of the intensity of the forward and backward field at time t, is already known from the previous procedure, so the carrier density equation is just a diffusion equation with a driving term and can be integrated very fast. An analysis of the work load of the program shows that nearly 80% of the time is spent in the Fourier transform routine.

Hexagons and rolls have been chosen as initial conditions for the simulations described in Sec. III, in order to shorten the transient. In all the other simulations the initial condition was a random perturbation of the uniform solution. In the region near threshold the random noise grows until bright spots appear and arrange themselves on an hexagonal grid (Fig. 7). This behavior is typical both of a focusing and a defocusing medium. In the latter case we can see that the spots at first arrange themselves on a square lattice, a symmetry induced by the grid, but after a short time the hexagonal structure becomes dominant. Figure 8 shows what happens to the field intensity in the stable hexagonal phase during the propagation from the slice to the mirror and back. In the case of the focusing medium the situation is rather trivial: the bright spots are focusing lenses that concentrate the field; diffraction then broadens the spots. In the defocusing case the bright spots are defocusing lenses and they diffuse the field, which has the appearance of a honeycomb. However, during propagation there is a crossover and the bright spots begin to appear and grow to dominance.

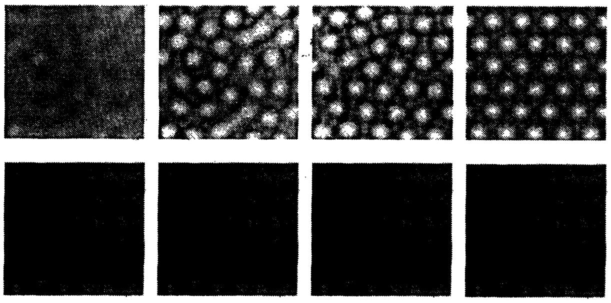

FIG. 7. Backward field intensity in a focusing (top) and a defocusing (bottom) medium. Gray scale, from white (high intensity) to black (low intensity), is used. Time increases from left to right. $R = 0.9$ and $t_R = 0.05$ in both cases. $\sigma = 1.0$ and $\chi = +1.0$ for the focusing medium, $\sigma = 0.5$ and $\chi = -1.0$ for the defocusing case.

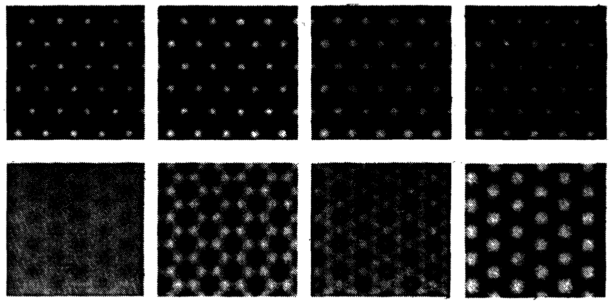

FIG. 8. Intensity of the field forming a stable hexagonal pattern as it propagates to the mirror and back in a focusing (top) and a defocusing (bottom) medium. Gray scale, from white (high intensity) to black (low intensity), is used. Time increases from left to right; the first image is the field intensity just after the slice, the last one just before going through it again. $R = 0.9$ and $t_R = 0.05$ in both cases. $\sigma = 1.0$ and $\chi = +1.0$ for the focusing medium, $\sigma = 0.5$ and $\chi = -1.0$ for the defocusing case.

In the analysis outlined in the two preceding paragraphs we have made the assumption the the most unstable wave vector is the dominant feature of the model dynamics, at least in the threshold region. To test this hypothesis we have averaged over the angle the power spectrum of an hexagonal structure similar to that shown in the top part of Fig. 7. The final result is the power spectrum as a function of the modulus of the wave vector $P(K)$. In Fig. 9 we have plotted the logarithm of $P(K)$ over the threshold curves; the most unstable wave vector is also the most intense, being roughly ten times greater than the second most important wave vector.

What happens as we increase the pump intensity? The nonlinear analysis says that the hexagonal structure is always stable, but this result is not correct. The hypothesis that the carrier density has just one Fourier component is acceptable near threshold: it is false at higher pump values. Generally speaking, for increasing values of the pump, the hexagonal structure becomes unstable and the

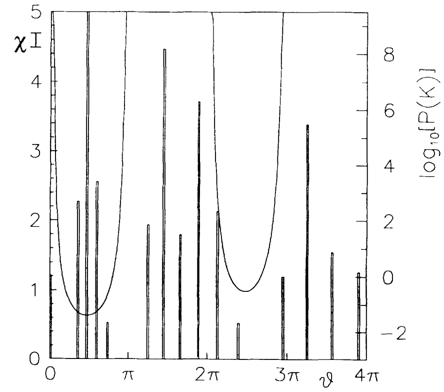

FIG. 9. Power spectrum of a hexagonal structure similar to that shown in the top part of Fig. 7 as a function of the modulus of the wave vector superimposed on the threshold curves. $R = 0.9$, $t_R = 0.05$, $\sigma = 10.0$, $\chi = +1$. Pump value is roughly 1.5 times the threshold.

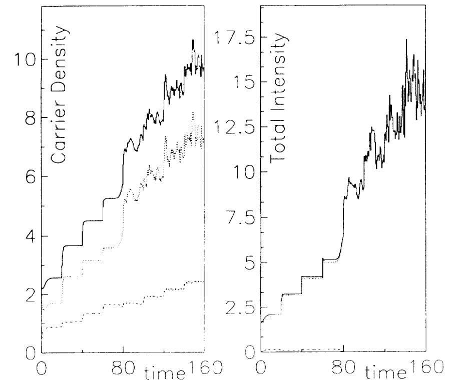

FIG. 10. Plot of the maximum (continuous line), minimum (dashed line), and modulation amplitude (dotted line) of the carrier density and total field intensity for various pump values. The pump is increased at regular intervals; the starting value is just above threshold, the final value is roughly three times the threshold. $R = 0.9$, $t_R = 0.05$, $\sigma = 10.0$, $\chi = 1.0$.

bright spots wobble around their position. If the pump is increased further the motion becomes more pronounced until the system reaches a state of spatiotemporal chaos. An example of such behavior is shown in Fig. 10; in this simulation we have increased the pump intensity every forty units of time from a value just above threshold to a value roughly three times threshold. In Fig. 10 we plot the extrema and the modulational amplitude of the carrier density on the left and of the total field intensity on the right. We can see that while for low pump power these two quantities reach an equilibrium, for high power they fluctuate without ever settling down. The details of this figure depend on the relative strength of diffusion versus diffraction.

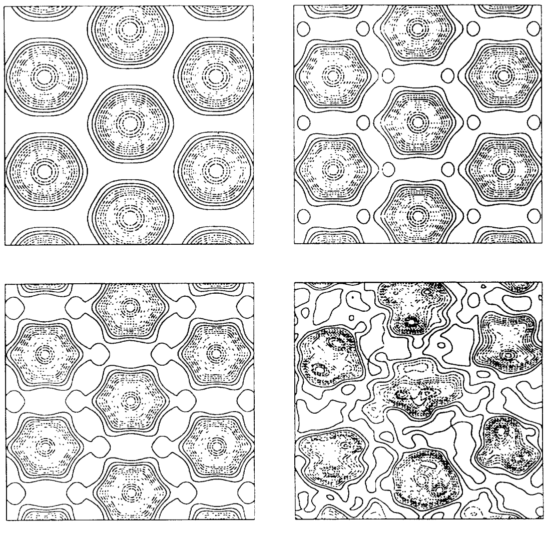

FIG. 11. Spot structure for various pump intensities in a case with weak diffusion. Contour plots of the carrier density are used. The four contour plots are a detail of the same region of the slice for $p \simeq \{1, 1.6, 1.8, 2.1\}$, respectively, from left to right, top to bottom. $R = 0.9$, $t_R = 0.05$, $\sigma = 10.0$, $\chi = +1.0$.

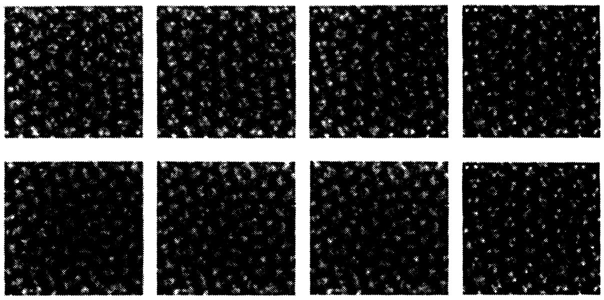

FIG. 12. Images of the carrier density in the case of turbulent dynamics and weak diffusion. In the top row $p = 2.3$ and the time interval between two successive images is 2.5; in the bottom row $p = 3.1$ and the time interval is 1.0. Same coding as in Fig. 7. $R = 0.9$, $t_R = 0.05$, $\sigma = 10.0$, $\chi = 10.0$.

Let us first analyze the case of small diffusion ($\sigma \gg 1$). Near threshold the spots are very smooth; as the intensity is increased, their edges become more steep. For higher pump values the spots acquire an inner structure, until they finally break down into small spots (see Fig. 11). These begin to wander around. Their motion gets more and more chaotic as the pump is increased to higher and higher values. In Fig. 12 we show four images of the carrier density at different times (from left to right) and for two different values of the pump (from top to bottom): in the top part of the picture the pump intensity is just above the threshold value for the hexagons' breakdown. The pattern has still an overall hexagonal symmetry even though the spots change position in time. In the bottom part of the picture the intensity is well above the instability threshold for the hexagons: the spots wander around faster than in the previous case and there is no trace of any symmetry.

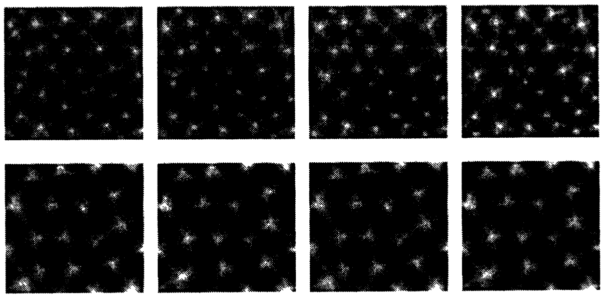

FIG. 13. Images of the carrier density in the case of turbulent dynamics and strong diffusion. In the top row $p \simeq 2$, in the bottom row $p \simeq 3$; the time interval between two successive images is 2.5 in both cases. Same coding as in Fig. 7. $R = 0.9$, $t_R = 0.05$, $\sigma = 0.1$, $\chi = 1.0$.

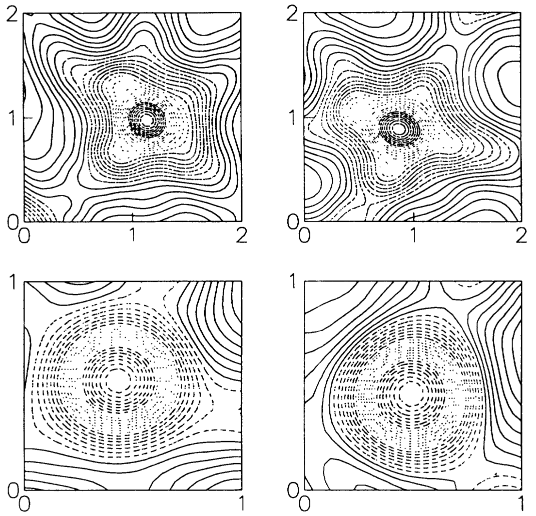

FIG. 14. Contour plots of two bright spots (top) and two gray spots (bottom). These spots were selected from the top right image shown in Fig. 13. The length units are scaled so that the gray spots have dimension 1. $R = 0.9$, $t_R = 0.05$, $\sigma = 0.1$.

If diffusion is large ($\sigma \ll 1$), instead, the bright spots do not change shape significantly with increasing input power. Diffusion washes out the details that were visible in the $\sigma = 10$ case. As the intensity is increased the spots become smaller and then begin to move. For values of the intensity roughly double the threshold (top of Fig. 13) there are two types of spots: bright and gray. All the spots on the slice seem to fall into one of these two categories; Fig. 14 shows the contour plots of two bright and two gray spots: both their shape and their height are the same. Moreover, the bright spots seem to interact one with the other by exchanging gray spots in a particlelike manner. All this suggests that we are looking at a coherent structure that is preserved in this turbulent motion. However we have not managed to put this "suggestion" in a more formal and rigorous framework. At higher values of the pump this phenomenon disappears: there is no trace left of the gray spots and the bright spots just move around quite independently one from the other (bottom part of Fig. 13).

We have given in this section an overview of the dynamical behavior of the Kerr slice with single feedback mirror: near the instability threshold for the plane-wave solution the system has a fixed point with a hexagonal symmetry, as predicted by the theory. As the intensity is increased to higher and higher values, the dynamics becomes turbulent; its main features in this phase are determined by the diffusion length. If it is small, the spots that were on the hexagonal structure fragment into smaller spots that wander around more and more rapidly as the intensity is increased. If the diffusion length is large, the spots just shrink a little, but do not fragment. In a window of pump values the dynamics seems to be dominated by the interaction of two kinds of spots, bright and gray. As the intensity is increased further, the gray spots disappear and we are left with only the bright ones.

V. CONCLUSIONS

In this work we have demonstrated that almost unlimited complexity can be generated from perhaps the simplest system which combines optical nonlinearity with extension in all three spatial dimensions. In particular, the fact that rolls are never stable in this model shows that suppression of the second transverse dimension for computational economy can result in predictions which are qualitatively in error over large domains of parameter space.

Given the richness of the complexity displayed in this model, the close similarity of the bifurcation structure to those found, for example, in fluid convection gives welcome guidance for analysis and interpretation. How far the analogy can be extended into the highly nonlinear and turbulent domains remains an open and interesting question. This is one of a number of interesting features and extensions of our model which remain to be explored.

Within the present model the effects of finite (Gaussian) beams need to be examined, both numerically and analytically. The effects of a curved feedback mirror (or equivalent lens-mirror combination) will enable closer comparison with past [7] and potential experiments. For defocusing media, the predicted regime of dominant $2t_R$ oscillation [2] remains completely unexplored. Detailed simulations of experiments will involve a more comprehensive set of properties for the nonlinear medium, including linear and nonlinear absorption and, in the case of such media as liquid crystals [9] and photorefractive materials [15], polarization and other vector properties.

Finally, it should be stressed that, even if the model proposed is unrealistically simple, it clearly demonstrates that space-time complexity in nonlinear optics does not require complex material response. Basic and universal phenomena such as the effect of propagation in converting phase modulation to amplitude modulation, in conjunction with some nonlinearity, are already sufficient to produce a huge variety of interesting phenomena.

ACKNOWLEDGMENTS

This work is supported in part by Science and Engineering Research Council Grants No. GR/F 49811, No. GR/F 76502, and No. GR/G 12665 and in part through a Twinning Project with the Science program of the European Communities.

[*] Also at Department of Physics, University of Heriot-Watt, Edinburgh, Scotland.

[1] N.B. Abraham and W.J. Firth, J. Opt. Soc. Am. B **7**, 951 (1990).

[2] W.J. Firth, J. Mod. Opt. **37**, 151 (1990).

[3] G. D'Alessandro and W.J. Firth, Phys. Rev. Lett. **66**, 2597 (1991).

[4] S. Ciliberto, P. Coullet, J. Lega, E. Pampaloni, and C. Perez-Garcia, Phys. Rev. Lett. **65**, 2370 (1990).

[5] Y. Pomeau, Physica D **23**, 3 (1986).

[6] G. Grynberg, E. Bihan, P. Verkerk, P. Simoneau, J.R.R. Leite, D. Bloch, S. Boiteux, and M. Ducloy, Opt. Commun. **67**, 363 (1988).

[7] G. Giusfredi, J.F. Valley, R. Pon, G. Khitrova, and H.M. Gibbs, J. Opt. Soc. Am. B **5**, 1181 (1988).

[8] W.J. Firth, A. Fitzgerald, and C. Paré, J. Opt. Soc. Am. B **7**, 1087 (1990).

[9] R. Macdonald and H.J. Eichler (unpublished).

[10] W.J. Firth and C. Paré, Opt. Lett. **13**, 1096 (1988).

[11] R.K. Dodd, J.C. Eilbeck, J.D. Gibbon, and H.C. Morris, *Solitons and Nonlinear Wave Equations* (Academic, Kilmarnock, 1982).

[12] L. Shtilman and G. Sivashinsky, Physica D **52**, 477 (1991).

[13] L. Shtilman and G. Sivashinsky, Can. J. Phys. **68**, 768 (1990).

[14] A.R. Gourlay, J. Inst. Math. Appl. **6**, 375 (1970).

[15] F.T. Arecchi, G. Giacomelli, P. Ramazza, and S. Residori, Phys. Rev. Lett. **65**, 2531 (1990).

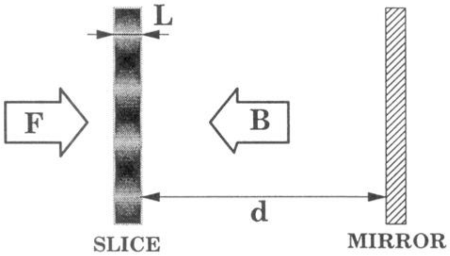

FIG. 1. Schematic diagram of the model. A thin slice of Kerr material, of thickness L, is illuminated from the left. The mirror, at a distance d, reflects this field back through the slice, thus closing the feedback loop.

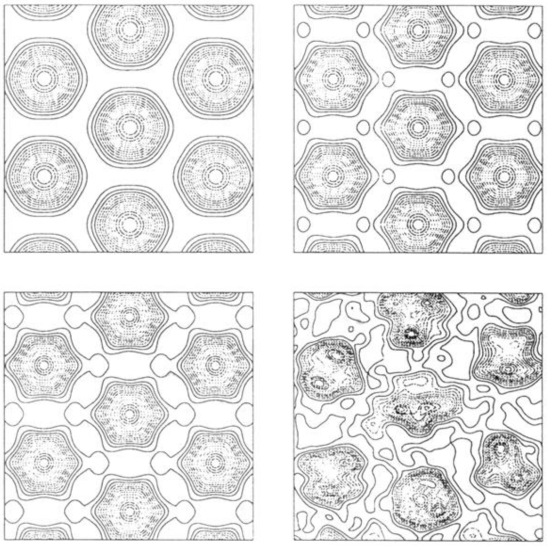

FIG. 11. Spot structure for various pump intensities in a case with weak diffusion. Contour plots of the carrier density are used. The four contour plots are a detail of the same region of the slice for $p \simeq \{1, 1.6, 1.8, 2.1\}$, respectively, from left to right, top to bottom. $R = 0.9$, $t_R = 0.05$, $\sigma = 10.0$, $\chi = +1.0$.

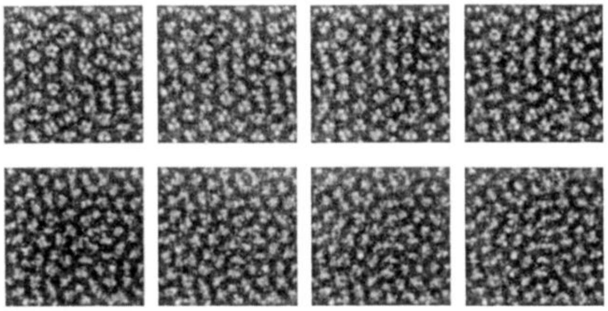

FIG. 12. Images of the carrier density in the case of turbulent dynamics and weak diffusion. In the top row $p = 2.3$ and the time interval between two successive images is 2.5; in the bottom row $p = 3.1$ and the time interval is 1.0. Same coding as in Fig. 7. $R = 0.9$, $t_R = 0.05$, $\sigma = 10.0$, $\chi = 10.0$.

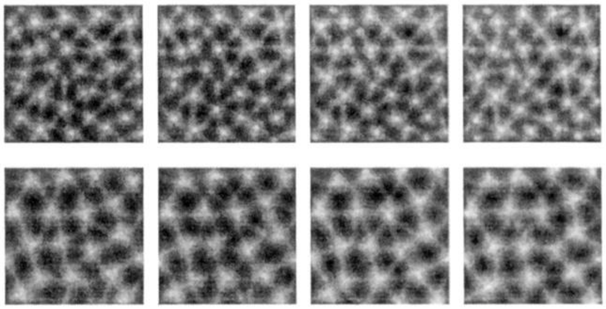

FIG. 13. Images of the carrier density in the case of turbulent dynamics and strong diffusion. In the top row $p \simeq 2$, in the bottom row $p \simeq 3$; the time interval between two successive images is 2.5 in both cases. Same coding as in Fig. 7. $R = 0.9$, $t_R = 0.05$, $\sigma = 0.1$, $\chi = 1.0$.

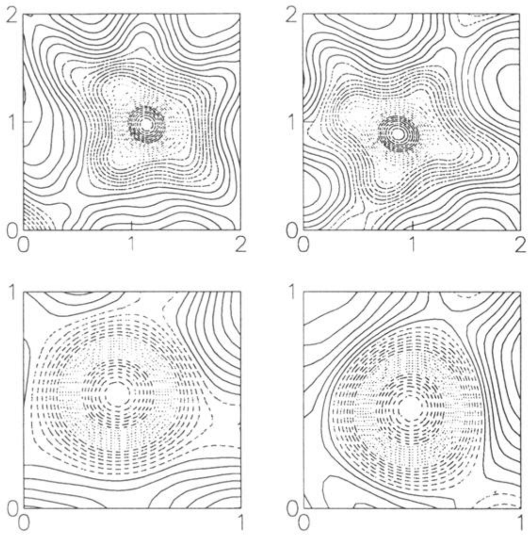

FIG. 14. Contour plots of two bright spots (top) and two gray spots (bottom). These spots were selected from the top right image shown in Fig. 13. The length units are scaled so that the gray spots have dimension 1. $R = 0.9$, $t_R = 0.05$, $\sigma = 0.1$.

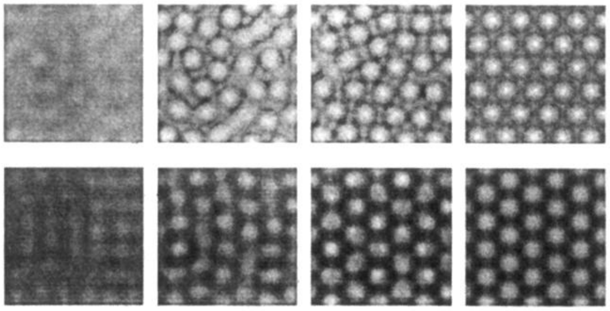

FIG. 7. Backward field intensity in a focusing (top) and a defocusing (bottom) medium. Gray scale, from white (high intensity) to black (low intensity), is used. Time increases from left to right. $R = 0.9$ and $t_R = 0.05$ in both cases. $\sigma = 1.0$ and $\chi = +1.0$ for the focusing medium, $\sigma = 0.5$ and $\chi = -1.0$ for the defocusing case.

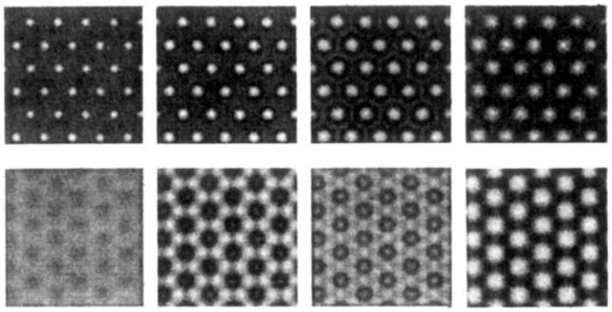

FIG. 8. Intensity of the field forming a stable hexagonal pattern as it propagates to the mirror and back in a focusing (top) and a defocusing (bottom) medium. Gray scale, from white (high intensity) to black (low intensity), is used. Time increases from left to right; the first image is the field intensity just after the slice, the last one just before going through it again. $R = 0.9$ and $t_R = 0.05$ in both cases. $\sigma = 1.0$ and $\chi = +1.0$ for the focusing medium, $\sigma = 0.5$ and $\chi = -1.0$ for the defocusing case.